PHYSICAL REVIEW D **85,** 062004 (2012)

Updated results from the RICE experiment and future prospects for ultra-high energy neutrino detection at the south pole

I. Kravchenko

University of Nebraska, Department of Physics and Astronomy, Lincoln, Nebraska, 68588-0299, USA

S. Hussain and D. Seckel

University of Delaware, Department of Physics and Astronomy and Bartol Research Institute, Newark, Delaware 19716, USA

D. Besson, E. Fensholt, J. Ralston, and J. Taylor

University of Kansas, Department of Physics and Astronomy, Lawrence, Kansas 66045-2151, USA

K. Ratzlaff and R. Young

University of Kansas, Instrumentation Design Laboratory, Lawrence, Kansas 66045-2151, USA

(Received 21 June 2011; revised manuscript received 8 November 2011; published 27 March 2012)

The RICE experiment seeks observation of ultra-high energy (UHE; $E_\nu > 10^{17}$ eV) neutrinos interacting in Antarctic ice, by measurement of the radio frequency (RF) Cherenkov radiation resulting from the collision of a neutrino with an ice molecule. RICE was initiated in 1999 as a first-generation prototype for an eventual, large-scale in-ice UHE neutrino detector. Herein, we present updated limits on the diffuse UHE neutrino flux, based on 12 years of data taken between 1999 and 2010. We find no convincing neutrino candidates, resulting in 95% confidence-level model-dependent limits on the flux $E_\nu^2 d\phi/dE_\nu < 0.5 \times 10^{-6}$ GeV/(cm^2 s-sr) in the energy range $10^{17} < E_\nu < 10^{20}$ eV, or approximately a twofold improvement over our previously published results. Recently, the focus of RICE science has shifted to studies of radio frequency ice properties as the RICE experimental hardware has been absorbed into a new experimental initiative (the Askaryan Radio Array, or "ARA") at the south pole. ARA seeks to improve on the RICE sensitivity by approximately 2 orders of magnitude by 2017 and thereby establish the cosmogenic neutrino flux. As detailed herein, RICE studies of Antarctic ice demonstrate that both birefringence and internal layer RF scattering result in no significant loss of ARA neutrino sensitivity, and, for the first time, verify *in situ* the decrease in attenuation length with depth into the Antarctic ice sheet.

DOI: 10.1103/PhysRevD.85.062004 PACS numbers: 14.60.Lm, 13.15.+g, 13.85.−t, 13.85.Tp

I. RADIOWAVE DETECTION OF NEUTRINOS

The RICE array is designed to detect events in which a neutrino-nucleon scattering event initiates a compact electromagnetic cascade in ice. Such cascades carry a net negative electric charge of magnitude 0.25 e/GeV, resulting in a pulse of radio Cherenkov emission via the "Askaryan effect" [1], with power peaked at wavelengths comparable to the lateral dimensions of the cascade, i.e., the Moliere radius (~ 10 cm). This paper reports new limits from the RICE array, updating the previous limits from 2006 [2], and also discusses how recent radio frequency (RF) studies of ice properties will impact new initiatives at the south pole.

Development of radio frequency detectors to measure ultra-high energy cosmic ray interactions has recently intensified. Projects use several methods and target materials including salt [3], ice [4–8] and lunar regolith [9,10]. Complementary efforts seek to measure the RF signals in cosmic ray-induced extensive air showers [11–14]. While calculations of RF signals from cosmic rays first appeared nearly 70 years ago [15], the new technology of nanosecond-scale digitizers and massive multichannel data analysis are now bringing the potential of radio detection to fruition.

A. Signal strength

Radio-wavelength detection of electromagnetic showers in ice relies on two experimentally established phenomena-long attenuation lengths exceeding 1 km, and coherence extending up to 1 GHz for Cherenkov emission. Discussions of the Askaryan effect [1] upon which the radio wave detection technique is founded, its experimental verification in a test beam environment [16,17], calculations of the expected radio-frequency signal from a purely electromagnetic shower [18–23], as well as hadronic showers [24], and modifications due to the LPM effect [25,26] can be found in the literature.

All estimates give the same qualitative conclusion-at large distances, the signal at the antenna inputs is a symmetric pulse, approximately 1–2 ns wide in the time domain. On the Cherenkov cone, the power spectrum rises monotonically with frequency, as expected in the coherent long-wavelength limit. In that limit, the excess negative charge in the shower front (roughly one electron per 4 GeV

shower energy) can be treated as a single (''coherent'') source charge. For perfect signal transmission (no cable signal losses) through an electrically matched system, calculations estimate the Cherenkov cone signal strength due to a 1 PeV neutrino initiating a shower at $R = 1$ km from an antenna to be $\sim 10\ \mu\mathrm{V}\sqrt{\mathrm{B}}$, with B the system bandwidth in GHz. This is comparable to the 300 K thermal noise over that bandwidth in the same antenna, prior to amplification.

II. THE RICE EXPERIMENT

Previous RICE publications described initial limits on the incident neutrino flux [27], calibration procedures [28], ice properties' measurements [29–31], and successor analyses of micro-black hole production [24], gamma-ray burst production of UHE neutrinos [32], tightened limits on the diffuse neutrino flux [2] and a search for magnetic monopoles [33]. Herein we update both our diffuse neutrino search, based on the entire data sample, using algorithms which differ minimally from our preceding search, and also provide new information derived from radioglaciological studies of the ice dielectric permittivity at radio wavelengths.

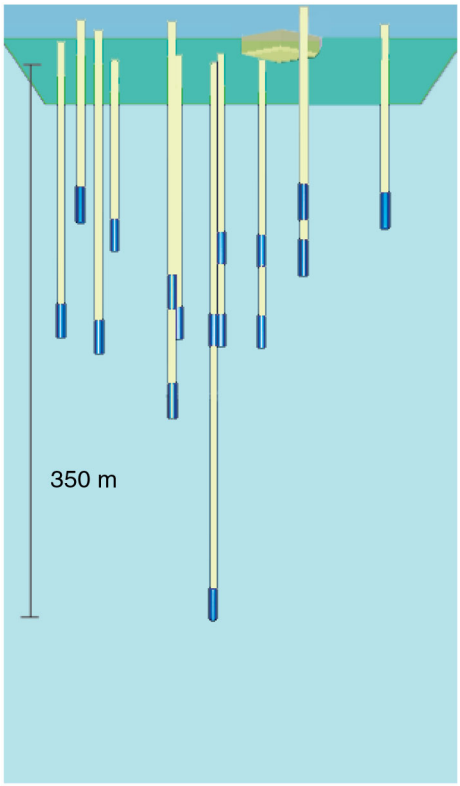

FIG. 1 (color online). Cutaway view of RICE experimental hardware. Fat dipole antennas (show in blue) are connected by coaxial cables (yellow) to a data acquisition system housed in the MAPO building (shown as rectangular solid). Locations are drawn to scale relative to MAPO. As indicated in the Figure, the deepest antenna is approximately 350 meters below the surface.

A. Experimental layout

Figure 1 shows the detector geometry (essentially unchanged since 2000) in relation to the Martin A. Pomerantz Observatory (MAPO) at the south pole station. The sensitive detector elements, radio receivers, are submerged at depths of several hundred meters close to the geographic south pole, in holes primarily drilled for the AMANDA experiment. Six of the RICE receivers are deployed in ''dry'' holes drilled specifically for RICE in 1998-99. Despite bulk motion of the ice sheet, and the closing of those dry holes under the ambient hydrostatic pressure over $\sim$5 years, we continue to receive signals from all successfully deployed antennas. A block diagram of the experiment, showing the signal path from in ice to the surface electronics, is shown in Fig. 2. The primary sensors are the in-ice ''fat dipoles'', which have good bandwidth over the frequency interval 200–1000 MHz, and a beam pattern consistent with the expected $\cos^2\theta$ dependence for wavelengths larger than the physical scale of the dipole antenna, as verified in transmitter tests (Fig. 3) performed while lowering a transmitter dipole antenna into a dry borehole.

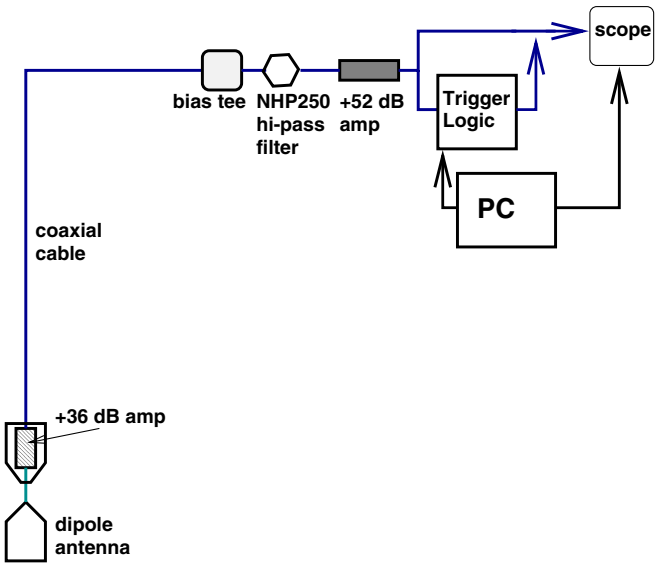

FIG. 2 (color online). Block diagram, showing primary experimental components. Beginning with the in-ice ''fat dipole'' antenna, signal is initially amplified, then conveyed by coaxial cable to the surface, where it is high-pass filtered, and then undergoes a second stage of amplification. Signals are then split into a ''trigger'' path and a ''digitization'' path; the latter of these brings signals into one channel of an HP5454 digital oscilloscope, which holds waveform data until the trigger decision is made (~1.5 μs). The trigger latch initiates readout of an 8.192 μs waveform sample, digitized at 1 GSa/s.

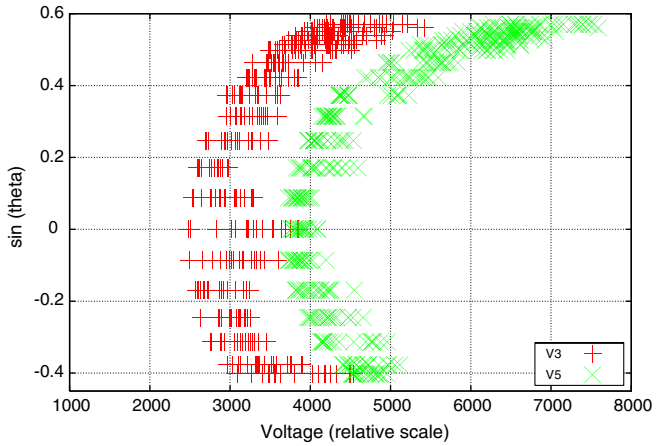

FIG. 3 (color online). Amplitude of received signal as a function of viewing angle between transmitter and receiver, for receiver channels 3 and 5 (selected on the basis of their ability to sample the largest range in $\sin\theta$). Dipole antennas, which are expected to follow a $\cos\theta$ field beam pattern should show a reduction in a factor of $2\,(\cos^2\theta/4)$ for broadcasts between two vertically aligned antennas, between $\sin\theta = 0$ and $\sin\theta = \sqrt{2}/2$, roughly consistent with observation.

B. Full data set

The statistics of the complete data taken thus far with the RICE array are summarized in Table I. Over a typical 24-hour period, roughly 1500 data event triggers pass a fast online hardware surface-background veto ("HSV"; with a decision time $\sim 5\ \mu$s/event) and an online software surface-background veto (~ 10 ms/event). To these data we have applied a sequence of offline cuts to remove background, as detailed below.

III. TRIGGER AND DATA COLLECTION

Our basic online procedures are essentially unchanged from our previous publication. The first three tiers, or trigger levels (Table II) are applied in either hardware (H) or software (S) online, as follows:

(1) L0: Passes hardware surface veto, with one antenna exceeding a threshold approximately equal to 6 times the ambient background noise level.
(2) L1: Four antennas satisfying an L0 requirement within a coincidence time window equal to the light transit time across the array (1.25 μs).
(3) L2: Events are deemed to be inconsistent with originating at the surface, using a software veto.

TABLE II. Summary of trigger rates at three levels. HSV refers to the online hardware surface veto of down-coming, anthropogenic noise. The third column represents the maximum trigger rate to process events exceeding the online event threshold. The final column represents the maximum rate at which data can be written to disk.

Trigger level	Requirement	Maximum rate	Typical winter rate
L0 (H)	Passes HSV veto	200 kHz	1 kHz
L1 (H)	Four antennas exceed threshold within 1.25 μs	100 Hz	1 Hz
L2 (S)	Passes surface-source veto	0.1 Hz	0.02 Hz

TABLE I. Summary of RICE data taken through December, 2010. "4-hit Triggers" refer to all events for which there are at least four RICE antennas registering voltages exceeding a preset discriminator threshold in a coincidence time comparable to the light transit time across the array (1.25 μs); "Unbiased Triggers" correspond to the total number of events taken at prespecified intervals and are intended to capture background conditions within the array; "Veto Triggers" are events tagged online by a fast (10 ms/event) software algorithm as consistent with having a surface origin. With the cessation of AMANDA operations in March, 2009, beginning in February 2010, the "AMANDA" trigger line was replaced by a 3-fold surface-antenna multiplicity trigger. Variations in the veto rate are attributed to the commissioning of new experiments, with associated anthropogenic electromagnetic interference, and also the decommissioning of other experiments, as well as communications streams such as the GOES satellite in 2006.

Year	Run Time (10^6 s)	Live Time (10^6 s)	4-hit Trigs ($\times 10^4$)	Unbiased ($\times 10^4$)	Vetoes ($\times 10^4$) (prescale)
1999	0.18	0.10	0.26	-	1.2 (1)
2000	22.3	15.7	30.6	3.3	11 182.8 (10000)
2001	4.6	3.3	6.0	1.3	317.4 (10 000)
2002	19.9	13.6	16.9	3.5	12 973.9 (10 000)
2003	24.5	17.1	13.8	4.4	3153.9 (10 000)
2004	11.6	9.4	9.4	2.5	142.5 (10 000)
2005	18.3	15.5	26.5	4.0	471.0 (10 000)
2006	19.3	16.5	8.9	4.2	20 560.5 (10 000)
2007	14.6	11.8	25.8	4.3	866.3 (10 000)
2008	20.1	17.2	21.1	5.0	186.2 (10 000)
2009	26.6	23.8	10.1	8.3	488.2 (10 000)
2010	23.1	21.9	6.1	5.5	224.4 (10 000)

Events passing all tiers are transferred daily from the south pole for permanent storage on disk at the University of Wisconsin.

IV. HIT FINDING AND EVENT RECONSTRUCTION

Our previous analysis assigned the hit time to the first $6 \times \sigma_V$ excursion in a waveform, with σ_V defined as the rms of the voltages recorded in the first 1000 ns of an event capture (i.e., prior to the possible onset of any signals). To improve our hit finding, we have performed a study of time domain signal characteristics. An ideal narrow-band antenna has a response to an impulse that follows the form:

$$V_0(t) \sim \cos(\omega_0 t) \exp(-t/\tau),$$

with $\tau \sim 1/\mathrm{B}$. For a first approximation to what these signals might look like, we used "thermal noise hits", defined as a sequence of waveform samples in unbiased events consistent with band-limited transients, drawn from the data itself. Figure 4 qualitatively indicates the reproducibility of such short-duration transient responses from channel-to-channel (2002 data), with the response to a sharp transmitter signal shown in Fig. 5 for comparison.

We have performed an embedding study to evaluate contributions to hit time resolutions and the relative efficacy of the damped exponential parametrization compared to previous hit time definitions. Monte Carlo simulations of neutrino-induced hits are embedded into data unbiased events, and the extracted hit times then compared with the known (true) embedded time. Our previous analysis employed the "first 6 σ_V excursion" hit criterion; based on Fig. 6 and the signals shapes displayed previously, we have now applied the more general "exponential ring" hit criterion, which records the time of waveforms exceeding 5.5 σ_V in voltage, and also have the shape of a damped exponential "ring". Monte Carlo simulations indicate that

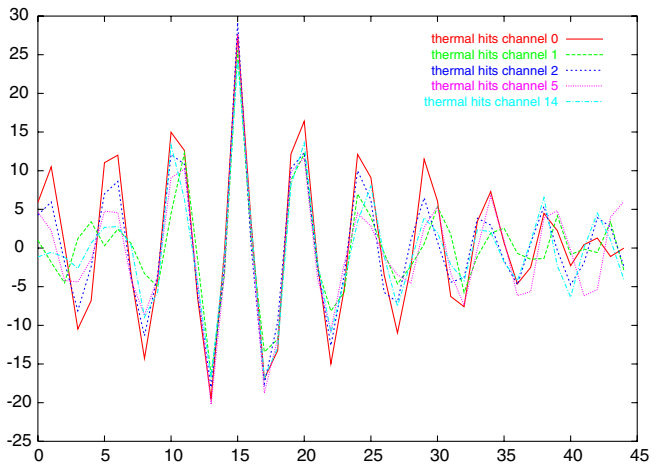

FIG. 4 (color online). "Short-duration" waveforms, selecting cases with fast impulsive responses (designated as "thermal hits"), for the indicated channels.

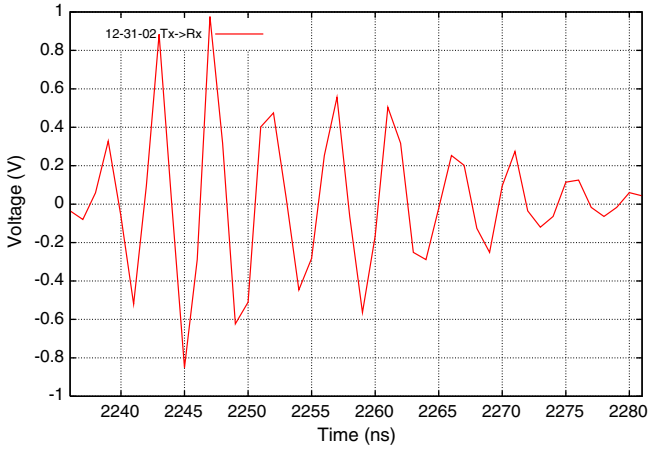

FIG. 5 (color online). Receiver waveforms captured when transmitter is active, for comparison with 'thermal' hits in previous Figure.

this improved timing resolution improves the azimuthal directional resolution of RICE by approximately 10%.

Such an algorithm is also designed to reject events where the signal persists for hundreds of nanoseconds in each channel. Figure 7 shows the time-over-threshold distribution, defined relative to the rms voltage σ_V, as the number of samples exceeding $\pm 6\ V_{\mathrm{rms}}$, for various triggers. The contamination of our "general trigger" data sample with large time-over-threshold events, which nearly uniformly trace to the surface, is evident from Fig. 7. Such waveforms are immediately rejected by requiring the expected damped exponential signal form. Also overlaid (green) is the distribution expected from Monte Carlo simulations, exhibiting a considerably

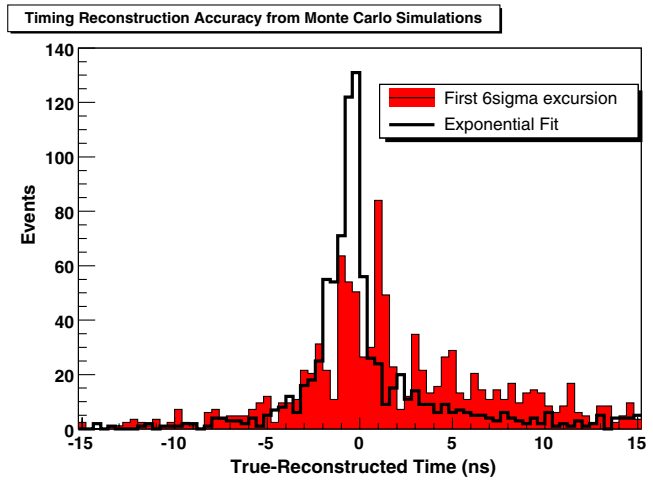

FIG. 6 (color online). Difference between the true (embedded) time between antenna hits minus the reconstructed hit time (after embedding) for two reconstruction algorithms. The indicated timing resolution due to pattern recognition uncertainties is approximately 2 ns.

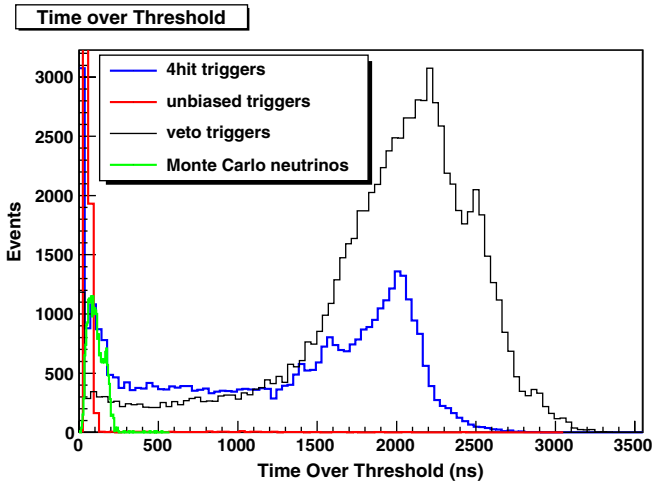

FIG. 7 (color online). "Time-over-threshold" for 2010 event triggers, by trigger type, as described in the text.

narrower distribution and clustered towards zero time-over-threshold.

V. BACKGROUNDS

Our previous publication [2] presented detailed consideration of anthropogenic transients, thermal noise backgrounds, and possible backgrounds from atmospheric muons, atmospheric neutrinos, air showers, and RF emissions due to solar flares. We herein briefly review techniques for background suppression.

We generally distinguish different backgrounds to the neutrino search according to the following criteria:

(i) vertex location of reconstructed source
(ii) waveform shape characteristics of hit channels (including, e.g., time-over-threshold [Fig. 7])
(iii) goodness-of-fit to a well-constrained single vertex as evidenced by timing residual characteristics (defined as the inconsistency of the recorded hit channels to originate from a single source point)
(iv) RF conditions during data-taking
(v) Fourier spectrum of hit channels
(vi) cleanliness of hits (e.g., presence of multiple pulses in an 8.192 μs waveform capture)
(vii) multiplicity of receiver antennas registering hits for a particular event

time-since-last-trigger ($\delta t_{ij} \equiv t_i - t_j$, where t_i is the time of the i th trigger and t_j is the time of the next trigger). In high-background, low-livetime instances, we expect $\delta t_{ij} \rightarrow \delta t_{\min}$, where $\delta t_{\min}$ is the $\sim$10 s/event readout time of the DAQ. In low-background, high-livetime instances, we expect $\delta t_{ij} \rightarrow \delta t_{\max}$, where $\delta t_{\max}$ is the ten-minute interval between successive unbiased triggers. We can coarsely characterize three general classes of backgrounds according to the above scheme, as follows.

(1) Continuous wave backgrounds (CW) have (a) a long time-over-threshold for channels with amplitudes well above the discriminator threshold, (b) large timing residuals (since the threshold crossing times will be ambiguous), (c) small values of δt_{ij} for the case where the discriminator threshold is far below the CW amplitude, (d) a Fourier spectrum dominated by one frequency (plus overtones), (e) a hit multiplicity which is on average roughly constant, and determined by the number of channels which exceed threshold when their noise voltage is added to the underlying CW voltage. Such backgrounds may cluster in time and are generally easily recognized online.
(2) True thermal noise backgrounds should have (a) - three-dimensional vertex locations which are spatially distributed as Gaussians peaked at the centroid of the array ($x = 0$, $y = 0$, $z = -120$ m), as demonstrated by Monte Carlo simulations (by simulating four hits at random times within the 1.25 μs discriminator window; see Fig. 8), (b) very small time-over-thresholds, (c) large timing residuals, (d) successive trigger time difference characteristics which depend in a statistically predictable way on the ratio of discriminator thresholds to rms background noise voltages, (e) a ratio of general/

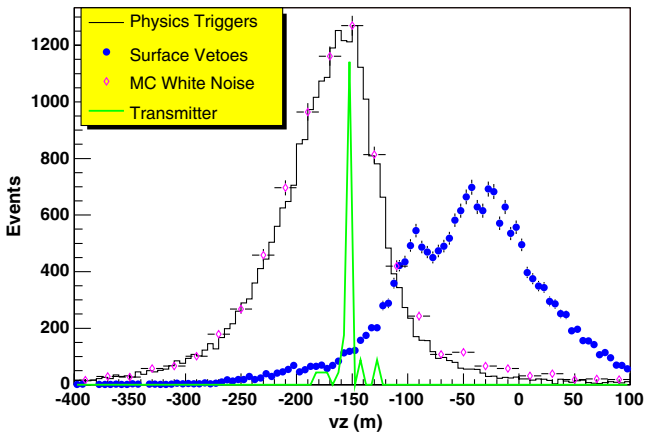

FIG. 8 (color online). Reconstructed source depth for primary neutrino search triggers ("physics triggers") compared to events identified as surface sources based on Hardware Surface Veto information, as well as transmitter calibration events (green) and simulated thermal noise (points). When anthropogenic backgrounds are low and the experiment is operating close to the thermal limit, the reconstructed vertex distribution for thermal noise events is expected to peak close to the center of the array, with a width given by the light transit distance across the 1.25 μs coincidence window defined by the RICE general event trigger. During the winter months, when station noise is typically lowest, approximately 50% of recorded events are thermal noise backgrounds. During the austral summer months, when human activity at the south pole station is largest, this fraction typically decreases to less than 10%.

unbiased triggers which, in principle, can be statistically derived from the background noise distribution observed in unbiased events, (f) a Fourier spectrum determined by the intrinsic band response of the various components of a RICE receiver circuit, (g) no double pulse characteristics, (h) no correlation with date or time.

(3) ''Loud'' transients are observed to constitute the dominant background. We subdivide possible transient sources into two categories: those sources which originate within the ice itself, primarily due to AMANDA and/or IceCube photomultiplier tube electronics, and those sources which originate on, or above the surface. After our initial deployment of three test antennas in 1996–97, high-pass (> 250 MHz) filters were inserted to suppress the former backgrounds, leaving more sporadic anthropogenic surface-generated noise as the dominant transient background. Such triggers are characterized by: (a) typically, large time-over-thresholds, (b) δt_{ij} distributions which reflect saturation of the DAQ data throughput, or show time structure if the source is periodic, (c) Fourier spectra which are likely to depart from thermal ''white'' noise in the frequency domain.

A. Vertex suppression of transient anthropogenic backgrounds

Vertex distributions give perhaps the most direct characterization of surface-generated ($Z \sim 0$) vs subsurface (and therefore, candidates for more interesting processes) events. Consistency between various source reconstruction algorithms gives confidence that the true source has been located. Because of ray tracing effects, it is difficult to identify surface sources at large polar angles, which increasingly fold into the region around the critical angle. We implement both a ''grid''-based χ^2 vertex search algorithm, as well as an analytic, 4-hit vertex reconstruction algorithm, as detailed previously [27]. We have additionally cross-checked our vertex-finding against results obtained using the CERN MINUIT package.

In our offline analysis, we require that the reconstructed vertex depth be greater than 200 meters to suppress anthropogenic surface noise.

B. Vertex quality requirements

We impose a maximum time residual (defined as the time deviation from consistency of the recorded antenna hit times with a single in-ice source point) requirement of less than 50 ns, per antenna hit. Since four antennas will necessarily allow a solution of the equation $\mathbf{r} = c(t - t_0)$, with t_0 the time of source emission, imposition of this requirement necessitates a minimum antenna hit multiplicity of five. This requirement is particularly effective at removing events where there may be a thermal noise fluctuation superimposed on anthropogenic noise, or multiple anthropogenic events which overlay upon each other.

C. Rejection of repetitive patterns

Inconsistency of the recorded hit time sequence with a previously logged hit time sequence, irrespective of the previous two requirements can also be used to identify backgrounds. This final requirement requires one full pass of each year's data to create a ''library'' of identified background hit time patterns, as follows. As each new event is processed, if the sequence of hit antennas for that event matches a previously recorded pattern to within 10 ns per antenna, then: (a) the event is considered to be ''repetitive'' and is discarded from further signal candidacy, and (b) the pattern itself is updated with a statistical weighting of the new event with all the previous events identified as consistent with that pattern. As a concrete example, an event with hit times in the first four antennas (exclusively) of 100, 250, 400, and 600 ns would be ''clustered'' with a previously logged pattern (with statistical weight 1) in the exact same channels with hit times of 92, 258, 403, and 605 ns, resulting in a modified ''clustered'' pattern, with statistical weight of 2, and reweighted hit times 96, 254, 401.5, and 602.5 ns.

The loss in neutrino efficiency incurred by this ''template cut'' algorithm is assessed by simulation to be of order 1%.

D. Air shower backgrounds

There are possible radio signals associated directly with cosmic ray air showers. These include the production of geo-synchrotron radiation in the atmosphere, as well as transition radiation and Cherenkov signals produced as the shower impacts and evolves into the ice. These three mechanisms all require coherent radiation from all or part of the shower. In all three cases, the transverse profile of the shower dictates a fundamental frequency response, whereas for the geo-synchrotron and Cherenkov signals the shower/observer geometry must also be favorable to have coherent emission from the full longitudinal development of the shower.

Coherent production of synchrotron radiation in the geomagnetic field has recently been observed by the LOPES [11], CODALEMA [12], AERA [13], and ANITA [14] collaborations. The coherent air shower signal is most intense below 100 MHz [34], but, as demonstrated by ANITA, still detectable in the RICE bandpass, which may attest to the observability of the air Cherenkov pulse that accompanies the geosynchrotron signal. We have not studied this mechanism in detail, but note that the frequency response is ultimately related to the geometry of the air shower—the signal rolls over at $f \sim cR/r_M^2$ where $R \sim 1$ km is the height of shower max and $r_M \sim$ 100–200 m is the Moliere radius for the shower.

Transition radiation results when the shower impacts the ice [35]. In this case, $R \sim 200$ m for RICE, $f \sim 200$ MHz, and the region for coherent emission is a disk of order 10 m radius. Only a fraction of the excess shower charge, typically 10%, is contained within that distance of the shower axis. Further, transition radiation is forward peaked, so illumination of more than one antenna string is rather unlikely. We have not seriously modeled transition radiation from air shower impacts as a background for RICE.

The most interesting signal for RICE is the Askaryan pulse produced when the air shower core hits the ice. At RICE frequencies, the Askaryan pulse must originate from a transverse dimension comparable to that for a shower initiated in ice, a few tens of cm at most. This length scale is compatible with the core of the shower where the highest energy particles reside. Particles have their last interactions of order 1 km above the ice, so the required relativistic $-\gamma$ factor is of order 10^4, corresponding to surface particle energies $\sim$10 GeV for e^-, e^+ and bremsstrahlung γ's.

We have run the standard RICE Monte Carlo simulation to assess the acceptance to impacting air shower cores. Simulated events illuminate the surface isotropically from the upper hemisphere over a distance within 500 meters of the center of the RICE array. At large zenith angles, the likelihood of four antennas being within some portion of the Cherenkov cone becomes large, however, the practical ability to separate such signals from surface background near the horizon is diminishingly small. Figure 9 displays the corresponding effective area, as a function of shower core energy, assuming the 10% shower core containment cited above. Given that the charged cosmic ray flux is approximately $1/5000$ m^2/yr at the nominal RICE event detection threshold of 100 PeV, and falling with an $E^{-2.7}$ power law (so that the integral flux falls as $E^{-1.7}$), Fig. 9 indicates that the expected detection rate per year for RICE is likely to be undetectably small.

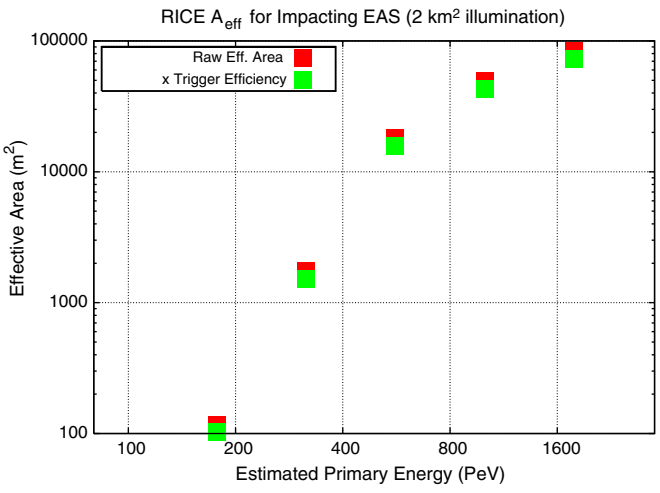

FIG. 9 (color online). Monte Carlo simulation results for the RICE effective area for air showers impacting the South Polar surface.

Such a possible signal was, in fact, explicitly rejected as consistent with down-coming anthropogenic noise, prior to 2009. In 2009, that veto was somewhat loosened, specifically to admit such possible signal. For this search, we required a "direct hit" corresponding to a vertex within 20 m of the center of the RICE array in order to have any opportunity at imaging the down-coming Cherenkov ring itself and thereby unambiguously discriminate against above-surface backgrounds; such backgrounds, at large zenith angles, will fold into a tight polar angle region around the critical angle $\theta_{\rm crit}$. Imposition of this fiducial requirement, of course, limits the effective area to a maximum of $\sim$1000 m^2.

For this search, all data were processed through a separate analysis chain with minimal initial event selection requirements consisting of: (i) a reconstructed impact point within that allowed fiducial area, (ii) good agreement between the two vertex finders, and (iii) a very loose "cut" on the goodness-of-fit to a Cherenkov cone, requiring that the event χ^2 be less than 100. These requirements allow only six event candidates in all of the 2009 data. Unfortunately, all six events fail subsequent time-over-threshold requirements on the waveform shape, resulting in no down-coming impacting air shower candidates.

E. Wind backgrounds

The extraordinary lack of moisture at the south pole, coupled with a volatile surface snow layer and an absence of large conductors to facilitate discharge of atmospheric electrostatic fields, results in extremely high atmospheric breakdown voltages from above-surface structures. Surface charge build-up can be enhanced by high wind velocities. Rapid discharges can subsequently produce measurable radio frequency signal. As demonstrated in Fig. 10, we observe an apparent correlation of trigger rate with wind velocity, as expected in a surface discharge model. Fortunately, these events typically trace back to the surface and do not pose an in-ice neutrino background.

F. Ambient (nonepisodic) radio frequency backgrounds at pole

The Very Low Frequency (VLF) [36] receiver array at the south pole is intended to monitor the ionosphere using a large set of buried antennas, at frequencies well below the RICE sensitivity. Nevertheless, the high power of the signal broadcast by this array can evidently couple into the electronics of the RICE data acquisition system, resulting in a measurable number of triggers (10.6% of all our physics triggers in 2010, e.g. [Fig. 11]). The waveforms in such events, however, immediately fail our exponential ring criterion in the offline analysis. The VLF background is by far the most pernicious of the periodic backgrounds observed to contaminate the RICE data sample.

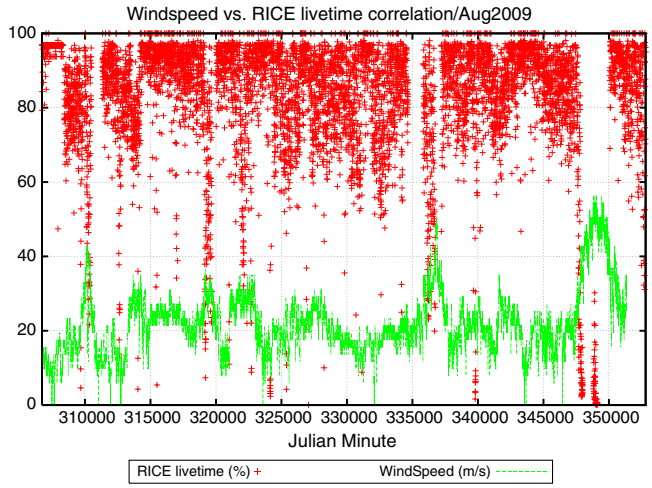

FIG. 10 (color online). Tabulated wind speed at the south pole (knots; green) vs RICE livetime (red). High wind speeds apparently result in large electrostatic discharge events from local above-surface structures. Such events are flagged offline as of nonneutrino origin.

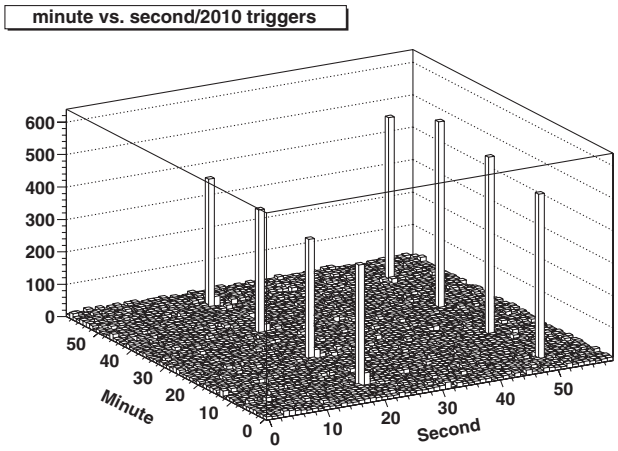

FIG. 11. Trigger time (second vs minute) showing the 15 min periodicity of the Very Low Frequency radar system, operating at 19.5 kHz, at the south pole.

VI. MONTE CARLO SIMULATIONS

We determine the neutrino detection efficiency of our event selection criteria using simulations of showers, both electromagnetic and hadronic, resulting from neutrino collisions, superimposed on environmental characterization drawn from data itself at random times (unbiased events). Our basic Monte Carlo simulation signal codes are unchanged since 2005, save for updates to modeling radio frequency ice dielectric response (detailed below). In practice, due to the Landau-Migdal-Pomeranchuk (LPM) effect, our sensitivity to neutrino interactions is dominated by the response to hadronic showers, and is therefore approximately uniform for all three neutrino flavors.

A. Event-finding efficiency

Our overall event-finding efficiency is approximately unchanged from our prior estimate. Of simulated events which we expect to trigger the RICE detector, we expect 74.2% to pass our primary event selection requirements. Cut-by-cut details are presented in Table III. Note that the definition of the cuts generally follows our previous analysis, with only slight differences.

B. Effective volume

As can be seen from Fig. 12, the overall neutrino response, as measured by effective volume, is essentially unchanged relative to our previous analysis. Systematic errors in effective volume, as indicated by the shaded band in Fig. 12, result in roughly a factor of 2 possible variation in the expected overall neutrino event yield. The breakdown of the contribution of various systematic uncertainties to our total systematic error is very similar to our previous analysis, with the exception of improvements in our understanding of ice properties, as outlined elsewhere in this document. These result in a net improvement

TABLE III. Cumulative Monte Carlo efficiency, using simulated neutrino events embedded into forced trigger events. Fractional efficiencies are measured relative to a total of 2500 simulated events, assuming 1:1:1 mix of ν_e:ν_μ:ν_τ, which passed our simulated trigger criteria. Also shown are event survival statistics for RICE data. Note that these event selection criteria are designed to encompass, and reject, all possible backgrounds itemized in the text, without necessarily targeting just one type.

Requirement	Efficiency (%)	Data events
Starting sample	100.0	2 298 921
$\geq$ 4 6-sigma hits	99.9	1 754 982
Maximum time-over-threshold cut	99.7	565 891
$\leq$ two channels with high time residual	98.0	145 723
Acceptable total time residual	95.5	38 922
Passes amplitude template cut	92.1	8035
Passes time template cut	89.1	1043
Vertex of at least one algorithm below firn	88.3	279
Agreement between two vertex-finding algorithms	85.1	140
Passes Cherenkov cone geometry cut	81.8	36
5 high quality $6\sigma_V$ hits	77.4	8
Deepest channel hit first	77.2	0
No surface antennas with good "early" hits	74.2	0

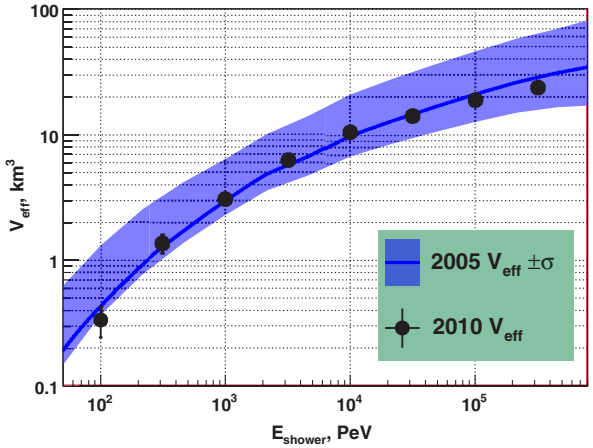

FIG. 12 (color online). Comparison of effective volume calculated with current Monte Carlo simulations with effective volume calculated for results reported in 2005.

of approximately 15% in total systematic error compared to our previous publication. Dominant systematic errors remain uncertainties in the attenuation length as well as uncertainties in the index-of-refraction profile through the firn. Figure 13 shows the relative contribution of various parameters to the overall systematic error. Shown are components due to uncertainties in the effective height (green), radio frequency attenuation length of the ice (cyan), uncertainties in the index-of-refraction (magenta, and dominant in the upper 200 m of the ice sheet), and also uncertainties due to the possibility of Cherenkov signals generated in ice, which reflect back down off the ice-air interface, and intercept the RICE array from above (yellow). Note that the latter effect, which can lead to so-called ''double'' hits, only increases the estimated effective volume, and is (conservatively) excluded from our calculation of the flux upper limit in the current analysis.

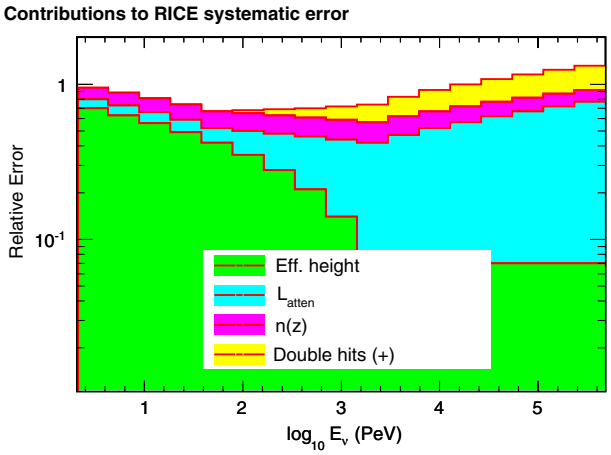

FIG. 13 (color online). Contribution to RICE systematic uncertainties in effective volume, as a function of energy, as detailed in the text.

VII. SEARCH FOR IN-ICE NEUTRINO INTERACTIONS AND DISCUSSION

Imposing the event selection requirements enumerated in Table III, we find that no events survive as in-ice shower candidates. One of the few events which satisfied all the waveform characteristic requirements, but was flagged as having surface origin is shown in Fig. 14.

Neutrino flux limit results

Our flux limit is derived directly from the effective volume $V_{\rm eff}$, the livetime $\mathcal{L}$, and the event-finding efficiency $\epsilon(\sim 0.64)$, which is the product of the online software veto efficiency ($\epsilon_{\rm online} \sim 0.91$) and the offline analysis efficiency ($\epsilon_{\rm offline} \sim 0.742$). Our 95% C. L. flux bounds are shown in Fig. 15. Compared to our previous result, we have slightly more than doubled our sensitivity. The dominating factor in our sensitivity gain is from extended livetime.

As can be immediately seen from inspection of Fig. 15, RICE is still well below the sensitivity required to conclusively probe the ''cosmogenic'' neutrino flux, expected from interactions of the ultra-high energy cosmic baryonic flux (protons, neutrons, or nuclei) with the cosmic microwave background (CMB). In brief, that flux is calculable by bootstrapping from the ultra-high energy charged cosmic ray particle flux at Earth, assuming some source composition (at the extremes, either proton or iron nuclei) for those measured charged cosmic rays, then integrating over redshift using some evolution model to obtain the anticipated rate in the current epoch. Using the parameters from the first such complete model [37], assuming an all-proton composition, and integrating over the RICE

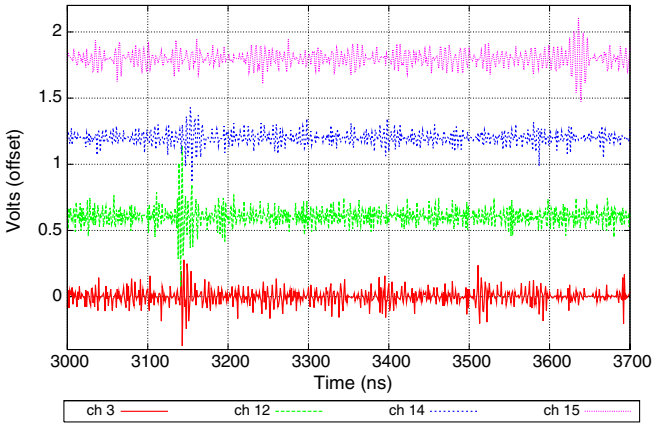

FIG. 14 (color online). Waveform display from event taken on Julian Day 93, UTC 02:45:41.407834.6 (2005). This event satisfies all event criteria listed in Table III, save for the requirement that the deepest channel (Ch. 15) have a hit time preceding, rather than following the other hits in the array. As can be seen from the Figure, the late impulse observed on Channel 15 marks this event as originating from the surface.

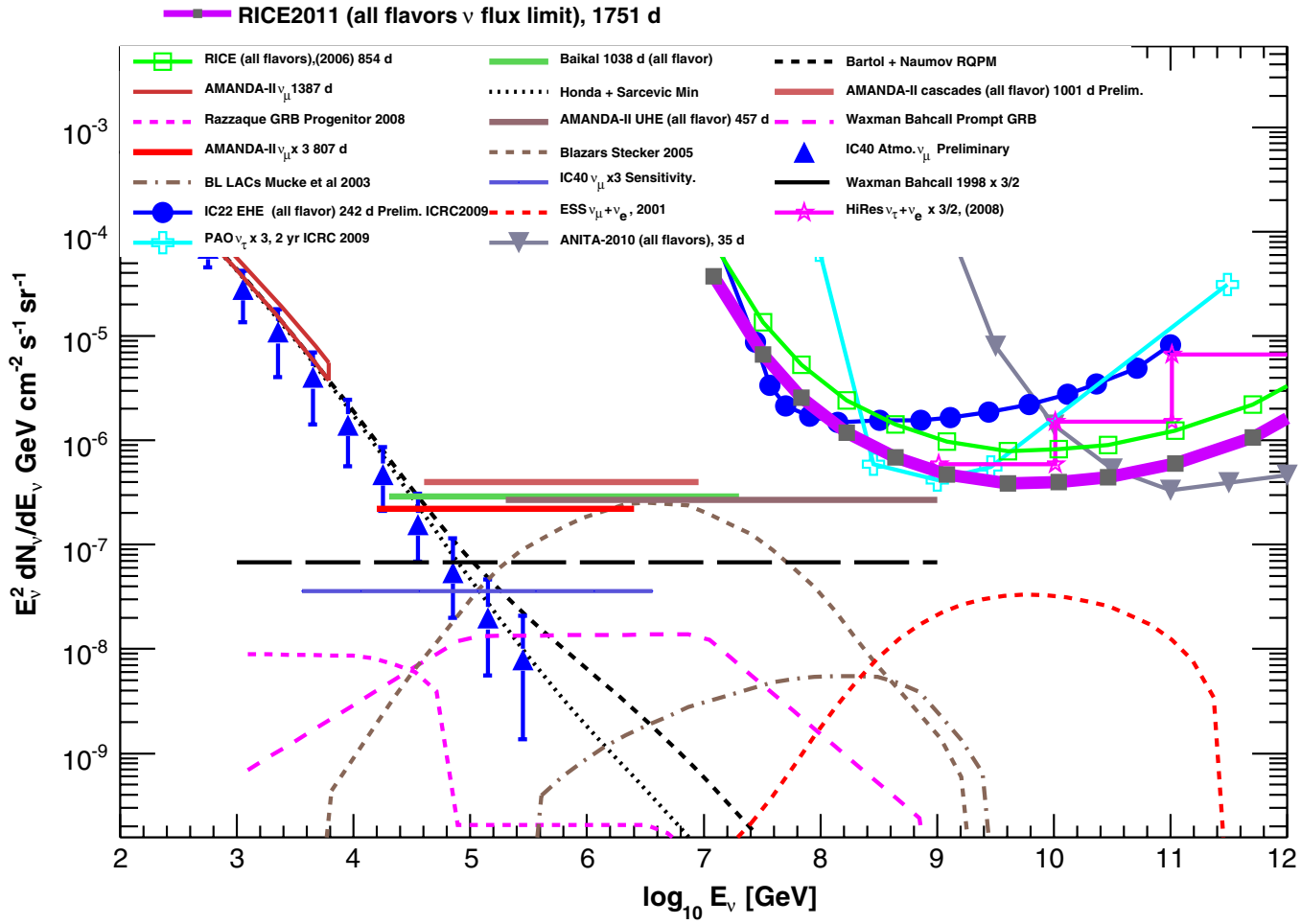

FIG. 15 (color online). Compilation of existing neutrino flux limits, including updates reported herein. Factors of 3 or $3/2$ shown in the plot are needed to translate predictions and experiments sensitive to only one or two neutrino flavors to the three flavors of neutrinos to which the RICE experiment is sensitive. Model predictions shown are from calculations of the neutrino fluence from blazars by Stecker [41], BL LAc galaxies [42], GRB's [43], photonuclear production of neutrinos by cosmic ray interactions with the cosmic microwave background [37], models of neutrinos generated locally to Earth [44–47] and active galactic nuclei influence predictions [48]. Other presented experimental limits are those from AMANDA-II [49–52], the previous RICE result [2], the HiRes experiment[53], based on electron neutrinos only (and extrapolated to three flavors), ANITAII [54] and a result from the Auger experiment [55], based on tau neutrinos only (and extrapolated to three flavors). Models are shown as dashed or solid lines; experimental results as lines/points.

sensitivity and livetime, we obtain an estimated number of 0.084 neutrino detections over the livetime quoted herein. Other recent estimates, which assume large admixtures of iron in the cosmic all-charged spectrum, result in estimated rates an order of magnitude smaller (0.0063 events [38]).

VIII. THE FUTURE OF IN-ICE UHE NEUTRINO DETECTION AT THE SOUTH POLE

Clearly, larger effective volumes are needed to definitively confront the entire suite of extant neutrino flux models. Synoptic strategies (ANITA, e.g.) afford sensitive volumes of 3×10^6 km^3, albeit viewed at typical distances of order 100–400 km from the event vertex, resulting in high neutrino detection thresholds due to the $1/R$ signal strength losses. In the embedded signal detection scheme (RICE, e.g.), the neutrino interaction vertex is typically "close", but the sensitive volume limited by the radio frequency ice attenuation length and the $\sim$2 km thickness of cold, high RF transparent ice, suggesting an "ideal" geometry of multiple "stations" of antennas deployed at shallow depths and separated by distances of order the radio attenuation length, each capable of independently imaging a neutrino interaction.

Central to the in-ice detection scheme are favorable radio frequency ice properties and transparency. By now, several measurements have redundantly established bulk ice attenuation lengths of order 1–2 km in the frequency

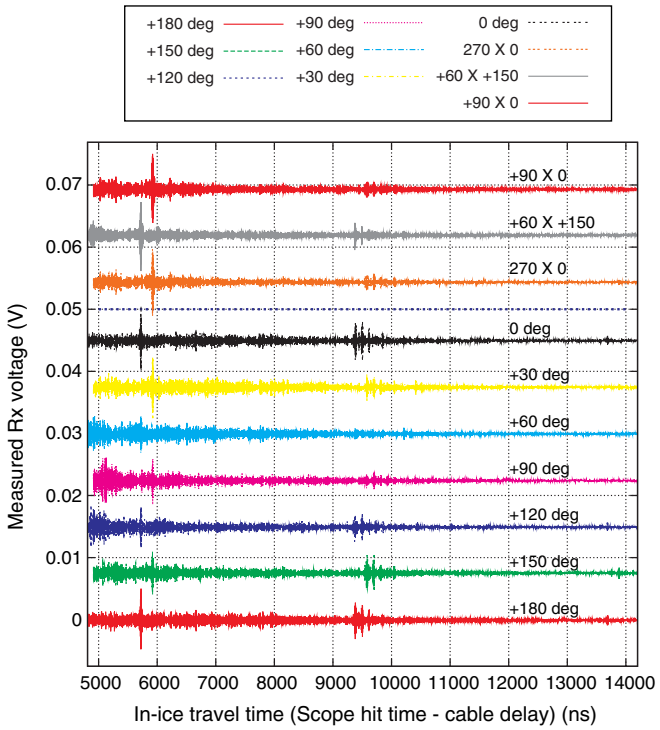

FIG. 16 (color online). Ensemble of internal layer radar reflections observed, as a function of E-field polarization plane of vertically broadcast radio signals. In this Figure, 40000 waveform captures have been averaged; the coordinate system used is a local coordinate system for which the ice flow axis makes an angle of 153° with respect to our zero degree convention. Azimuthal polarization angle is shown in the key; also included are "cross-polarized" ($+60 \times +150$) orientation results, for which transmitter and receiver horn are orthogonal to each other. Echo time is shown horizontally, and approximately translates to depth via: depth [km] $\approx$ t[ns]/12000. For visual clarity, successive vertical traces have been offset by ± 100 ns; reflection structure is actually synchronous to within 1 ns.

range of interest. Within the last 2–3 years, as relative gains in neutrino sensitivity diminished, and in anticipation of a next-generation successor experiment, the RICE mission has begun to focus on precise characterization of asymmetries in-ice properties, particularly effects of internal scattering layers and inherent asymmetries in the single-ice-crystal dielectric tensor. Both of these can be probed using bistatic radar echo sounding techniques. In this approach, a high-gain transmitter horn antenna is placed at one location on the snow surface, and the internal reflections from both within the snow, as well as the bedrock, are recorded by a second high-gain receiver horn antenna. Geometric asymmetries in the ice response can be studied by rotating the azimuthal plane of polarization of the horn antennas.

Figures 16 and 17 show the measured reflections for times prior (Fig. 16) and corresponding (Fig. 17) to the expected time for the bedrock echo, at a depth of 2850 m. Both show strong dependence of received signal with broadcast azimuthal angle, although only the latter shows the time delay between two polarizations indicative of a difference in index-of-refraction with orientation, i.e., birefringence. Quantitatively, the echo amplitudes observed from internal reflections are typically 20–40 dB reduced compared to those expected from a "perfect mirror", consistent with the characteristics of reflections from acid layers embedded within the ice itself. Frequency analysis of those reflections additionally corroborate the expected $1/f$ amplitude dependence of acid layer reflections. Note that, for both these Figures, we have averaged over 10 K–40 K waveform captures to enhance the signal-to-noise ratio, corresponding to a reduction in the incoherent noise by (typically) at least 2 orders of magnitude. None of these reflections would therefore be visible in a single "event", such as an in-ice neutrino interaction.

Lab studies have shown that completely aligned ice crystals convey radio waves with approximately 1.7% reduced speeds for propagation transverse to the plane containing that crystal (the $\hat{c}$ axis). The time lag between the top three traces vs the bottom three traces shown in Fig. 17 corresponds to approximately 50 ns, over a total propagation time of 34000 ns, i.e., a birefringent asymmetry of order 0.15% between wave speed propagation along the ordinary (fast-) vs extraordinary (slow-) axes. We can additionally use the *lack* of any asymmetry observed in Fig. 16 to conclude that birefringence is a feature only of the lower (warmer) half of the ice sheet at the south pole, at a level of 0.25% asymmetry. Taken together, these results indicate that losses due to internal radio layers will not result in appreciable loss of signal for neutrino-induced radio signals received in future experiments, and also that diminution of peak signal strength due to birefringence will similarly be noticeable in only $\sim$5% of all neutrino detection geometries.

Somewhat interestingly, Fig. 16 shows a marked dependence of peak measured reflected amplitude, as a function of azimuth. Given that the only "preferred" horizontal direction is defined by the ice flow axis, it is natural to consider correlations between the amplitude variations observed in both the internal layer and also bedrock reflections, with the known bulk motion of the ice sheet. Figure 18 shows a strong correlation in three of the five most prominent observed internal layer echoes with the ice sheet flow direction and suggests that the internal acid layers are likely aligned (similar to a diffraction grating) by the local ice flow.

A. Dependence of attenuation length with depth

The observed echo amplitudes shown in Fig. 16 are largely determined by three factors: the intrinsic reflectivity of each layer, the diminution of signal power P_{signal} with distance, and attenuation of the signal due to ice

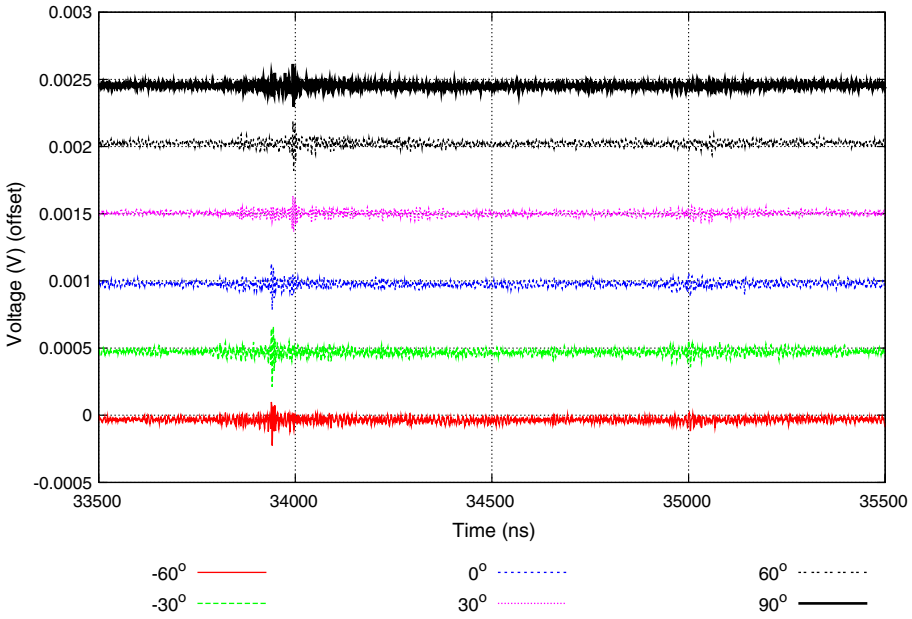

FIG. 17 (color online). Ensemble of bedrock radar reflections observed, as a function of E-field polarization plane of vertically broadcast radio signals.

absorption. For the directional horn antennas used in this experiment, $P_{\text{signal}} \propto r^{-\alpha}$, with $1 < \alpha < 2$. If we assume approximately equivalent reflection coefficients for all observed internal layers, we can determine a "local" amplitude attenuation length between the first three, and last three layers, as shown in Table IV, by direct application of the Friis equation [39], and using the azimuth-averaged values of amplitude. For this calculation, we take $\alpha = 2$; assuming a cylindrical-flux tube with no transverse spreading ($\alpha = 1$) gives values approximately 20% smaller than those presented in Table IV. Our calculations are consistent with the expected warming of the ice sheet from the bedrock below, and the corresponding reduction in attenuation length with increasing temperature.

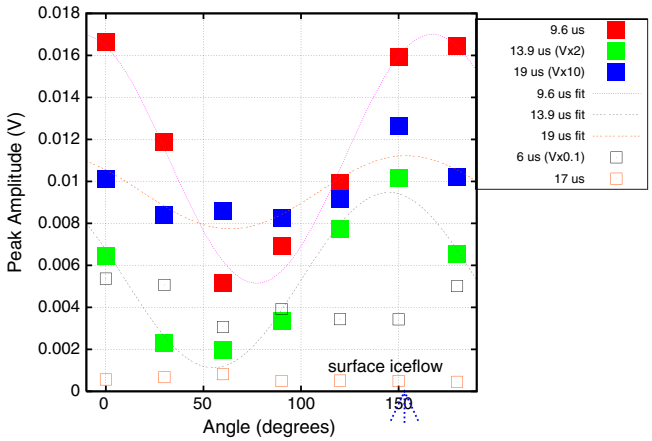

FIG. 18 (color online). Peak amplitude dependence of internal layer reflection, indexed by echo time, as a function of signal polarization. Note the correlation of phase with the direction of local ice flow direction, indicated by the dashed blue arrow.

B. Future plans for radioglaciology

Thus far, virtually all information on the radio frequency response of ice sheets has been derived using vertically broadcast signals. In the austral summer of 2011–12, RICE hardware will be used to broadcast RF at largely oblique angles, which will provide information on the ice response away from the $\hat{c}$ axis, and more typical of the geometry of the neutrino signals to be detected by in-ice experiments such as RICE. As illustrated above, all RICE studies done thus far, however, substantiate the basic premise of such detectors: that the excellent RF properties of cold polar ice imply that englacial neutrino detectors provide the most

TABLE IV. Interlayer attenuation lengths, calculated from amplitudes measured for returns, and assuming uniform reflectivity of all layers, as discussed in text. Estimated systematic errors are of order 25–30%. First column indicates first reflecting layer; successive columns indicate second reflecting layer used to calculate attenuation length via Friis Equation. These results affirm the expectation that primary neutrino sensitivity is poorest in the warm ice near the bedrock.

	13.9 μs	17.2 μs	19.6 μs
6 μs	3348 m	1521 m	1514 m
9.6 μs	1170 m	867 m	964 m
13.9 μs		643 m	849 m

cost effective technique for confronting the cosmogenic neutrino flux.

C. The ARA experimental initiative

During the austral summer of 2010–11, initial deployments of the next generation of neutrino detection hardware, realized as the recently funded Askaryan Radio Array (ARA [40]), were made at the south pole. The first ARA deployment, in the form of a relatively shallow (20–30 m) ''test bed'' prototype has already demonstrated 20 arc-minute angular reconstruction of calibration antennas, as well as sensitivity to variations in the received galactic noise and RF emissions from solar flares. An ambitious proposal, including 14 institutions from eight countries has been submitted to develop an autonomously-powered (and therefore, arbitrarily scalable) experiment capable of initially defining the cosmogenic neutrino flux, and, over the time scale of a decade, eventually performing statistical characterization of that flux.

Comprising 37 stations, each individually with an energy reach approximately an order of magnitude below that of RICE, ARA will achieve an improvement of greater than 2 orders of magnitude in total effective volume, achieved via:

(1) direct digitization at the sensor (antenna) rather than on the surface, eliminating the ~15 dB signal losses typically incurred by conveyance through coaxial cable.
(2) order-of-magnitude reduction of the geometric scale of each ''station'' from the 200-m typical of RICE such that the temporal signal coincidence window can similarly be narrowed by a comparable factor of 10.
(3) Siting of the experiment several km from the main south pole station itself, resulting in considerably lower ambient noise rates. The remote ARA deployment site exhibits virtually none of the anthropogenic, or wind-generated RFI that plagued the RICE data sample.
(4) Extension of the lower-frequency limit of the antenna response from the current 250 MHz to ~150 MHz, resulting in improved response to off-Cherenkov-peak signals.
(5) ''Optimized'' antenna receiver placement, as opposed to the requirement that RICE co-deploy in boreholes being drilled for the AMANDA experiment.

The 2011–12 austral season will include the first deployment of a full-fledged ARA station (''ARA-1''); that single station will, in 1 yr, have equivalent neutrino sensitivity to the ten years of RICE data accumulated thus far and reported herein. The first results on neutrino searches from the ARA testbed should be forthcoming within the next few months.

ACKNOWLEDGMENTS

The authors particularly thank C.Allen (University of Kansas) for very helpful discussions, as well as our colleagues on the RICE and ANITA experiments. We also thank A. Bricker of Lawrence High School (Lawrence, KS) for his assistance in working with the Lawrence and Free State High School students. We also thank the winterovers at the south pole station (Xinhua Bai, The Most Rev. A. Baker, P. Braughton, C. Hammock, M. Offenbacher, M. Noske, N. Hart-Michel, R. Fuhrman, F. Hamblin, and N. Strehl) whose efforts were essential to the operation of this experiment. S. Grullon contributed the ROOT software code used to produce the upper limit compilation presented in this article. This work was supported by the National Science Foundation's Office of Polar Programs under Grant No. OPP-0826747 and the QuarkNet programs.

[1] G. A. Askaryan, Zh. Eksp. Teor. Fiz. **41**, 616 (1961); Sov. Phys. JETP **14**, 441 (1962).
[2] I. Kravchenko *et al.* (RICE Collaboration), Phys. Rev. D **73**, 082002 (2006).
[3] P. Gorham D. Saltzberg, A. Odian, D. Williams, D. Besson, G. Frichter, and S. Tantawi, Nucl. Instrum. Methods Phys. Res., Sect. A **490**, 476 (2002); R. Milincic P. W. Gorham, D. Saltzberg, R. C. Field, G. Guillian, D. Walz, and D. Williams arXiv:astro-ph/0503353.
[4] A. Butkevich *et al.*, Fiz. Elem. Chastits At. Yadra **29**, 660 (1998); , , , , , and , Phys. Part. Nucl. **29**, 266 (1998).
[5] L. Gerhardt *et al.*, Nucl. Instrum. Methods Phys. Res., Sect. A **624**, 85 (2010).
[6] P. W. Gorham *et al.*, Astropart. Phys. **32**, 10 (2009).
[7] N. Lehtinen *et al.*, Phys. Rev. D **69**, 013008 (2004).
[8] D. Besson, Dagkesamanskii, E. Kravchenko, I. Kravchenko, and I. Zheleznykh, Nucl. Instrum. Methods Phys. Res., Sect. A **662**, S50 (2012).
[9] P. Gorham *et al.*, Phys. Rev. Lett. **93**, 041101 (2004).
[10] C. W. James *et al.*, Phys. Rev. D **81**, 042003 (2010).
[11] J. Hoerandel *et al.*, Nucl. Instrum. Methods Phys. Res., Sect. A **630**, 171 (2011).
[12] D. Ardouin *et al.*, Int. J. Mod. Phys. A **20**, 6869 (2005).
[13] P. Abreu *et al.*, Nucl. Instrum. Methods Phys. Res., Sect. A **635**, 92 (2011)
[14] S. Hoover *et al.*, Phys. Rev. Lett. **105**, 151101 (2010).
[15] P. M. S. Blackett and A. C. B. Lovell, Proc. R. Soc. A **177**, 183 (1941).

[16] D. Saltzberg *et al.*, Phys. Rev. Lett. **86**, 2802 (2001).
[17] P. Gorham *et al.*, Phys. Rev. D **72**, 023002 (2005).
[18] E. Zas, F. Halzen, and T. Stanev, Phys. Lett. B **257**, 432 (1991); E. Zas, F. Halzen, and T. Stanev, Phys. Rev. D **45**, 362 (1992).
[19] J. Alvarez-Muniz E. Marqués, R. A. Vázquez, and E. Zas, Phys. Rev. D **68**, 043001 (2003); J. Alvarez-Muniz, R. A. Vázquez, and E. ZasPhys. Rev. D **62**, 063001 (2000); J. Alvarez-Muniz E. Marqués, R. A. Vázquez, and E. Zas **74**, 023007 (2006).
[20] S. Razzaque *et al.*, Phys. Rev. D **65**, 103002 (2002).
[21] S. Razzaque *et al.*, Phys. Rev. D **69**, 047101 (2004).
[22] R. V. Buniy and J. P. Ralston, Phys. Rev. D **65**, 016003 (2001).
[23] J. Alvarez-Muniz, A. Romero-Wolf, and E. Zas, Phys. Rev. D **84**, 103003 (2011).
[24] S. Hussain and D. McKay, Phys. Rev. D **70**, 103003 (2004).
[25] L. D. Landau and I. J. Pomeranchuk, Dokl. Akad. Nauk SSSR **92**, 535 (1953); **92**, 735 (1953); A. B. Migdal, Phys. Rev. **103**, 1811 (1956); J. Alvarez-Muñiz, R. A. Vázquez, and E. Zas, Phys. Rev. D **61**, 023001 (1999).
[26] S. Mandal, S. Klein, and J. D. Jackson, Phys. Rev. D **72**, 093003 (2005).
[27] I. Kravchenko *et al.*, Astropart. Phys. **19**, 15 (2003).
[28] I. Kravchenko *et al.*, Astropart. Phys. **20**, 195 (2003).
[29] I. Kravchenko, D. Besson, and J. Meyers, J. Glaciol. **50**, 522 (2004).
[30] D. Besson, R. Keast, and R. Velasco, Astropart. Phys. **31**, 348 (2009).
[31] I. Kravchenko *et al.*, Astropart. Phys. **34**, 755 (2011).
[32] D. Besson *et al.*, Astropart. Phys. **26**, 367 (2007).
[33] D. P. Hogan *et al.*, Phys. Rev. D **78**, 075031 (2008).
[34] T. Huege and H Falcke, Astropart. Phys. **24**, 116 (2005).
[35] E. D. Gazazian, K. A. Ispirian, and A. S. Vardanyan, AIP Conf. Proc. **579**, 111 (2001).
[36] http://www-star.stanford.edu/~vlf/south_pole/south%20pole.htm.
[37] R. Engel, D. Seckel, and T. Stanev, Phys. Rev. D **64**, 093010 (2001).
[38] K. Kotera, D. Allard, and A. V. Olinto, J. Cosmol. Astropart. Phys. 10 (2010) 013.
[39] http://en.wikipedia.org/wiki/Friis_transmission_equation.
[40] P. Allison *et al.* (ARA Collaboration), Astropart. Phys. **35**, 457 (2012).
[41] F. W. Stecker, Phys. Rev. D **72**, 107301 (2005).
[42] A. Mucke *et al.*, Astropart. Phys. **18**, 593 (2003).
[43] S. Razzaque, P. Meszaros, and E. Waxman, Phys. Rev. D **68**, 083001 (2003).
[44] Enberg, Reno, and Sarcevic, Phys. Rev. D **78**, 043005 (2008).
[45] G. Fiorentini, V. A. Naumov, and F. L. Villante, Phys. Lett. B **510**, 173 (2001).
[46] T. Gaisser *et al.*, Phys. Rev. D **70**, 023006 (2004).
[47] Honda *et al.*, Phys. Rev. D **75**, 043006 (2007).
[48] J. Becker, Biermann, and Rhode, Astropart. Phys. **23**, 355 (2005).
[49] R. Abassi *et al.*, Phys. Rev. D **79**, 102005 (2009).
[50] R. Abbasi (IceCube Collaboration) *et al.*, Astropart. Phys. **34**, 48 (2010).
[51] A. Achterberg *et al.*, Phys. Rev. D **76**, 042008 (2007).
[52] M. Ackerman *et al.*, Astrophys. J. **675**, 1014 (2008).
[53] R. U. Abbasi *et al.*, Astrophys. J. **684**, 790 (2008).
[54] P. W. Gorham *et al.*, Phys. Rev. D **82**, 022004 (2010); P. W. Gorham *et al.*, Phys. Rev. D **85**, 049901 (2012).
[55] J. Abraham *et al.*, Phys. Rev. D **79**, 102001 (2009).